ORNL/TM-2016/229

Computational Thermodynamics Aided Design of Novel Ferritic Alloys

Ying Yang
Tianyi Chen
Lizhen Tan

Approved for public release.
Distribution is unlimited.

June 30, 2016

OAK RIDGE NATIONAL LABORATORY
MANAGED BY UT-BATTELLE FOR THE US DEPARTMENT OF ENERGY

DOCUMENT AVAILABILITY

Reports produced after January 1, 1996, are generally available free via US Department of Energy (DOE) SciTech Connect.

Website http://www.osti.gov/scitech/

Reports produced before January 1, 1996, may be purchased by members of the public from the following source:

National Technical Information Service
5285 Port Royal Road
Springfield, VA 22161
Telephone 703-605-6000 (1-800-553-6847)
TDD 703-487-4639
Fax 703-605-6900
E-mail info@ntis.gov
Website http://www.ntis.gov/help/ordermethods.aspx

Reports are available to DOE employees, DOE contractors, Energy Technology Data Exchange representatives, and International Nuclear Information System representatives from the following source:

Office of Scientific and Technical Information
PO Box 62
Oak Ridge, TN 37831
Telephone 865-576-8401
Fax 865-576-5728
E-mail reports@osti.gov
Website http://www.osti.gov/contact.html

This report was prepared as an account of work sponsored by an agency of the United States Government. Neither the United States Government nor any agency thereof, nor any of their employees, makes any warranty, express or implied, or assumes any legal liability or responsibility for the accuracy, completeness, or usefulness of any information, apparatus, product, or process disclosed, or represents that its use would not infringe privately owned rights. Reference herein to any specific commercial product, process, or service by trade name, trademark, manufacturer, or otherwise, does not necessarily constitute or imply its endorsement, recommendation, or favoring by the United States Government or any agency thereof. The views and opinions of authors expressed herein do not necessarily state or reflect those of the United States Government or any agency thereof.

ORNL/TM-2016/229
M3CA-15-TN-OR0402027

Nuclear Energy Enabling Technologies (NEET): Reactor Materials

COMPUTATIONAL THERMODYNAMICS AIDED DESIGN OF NOVEL FERRITIC ALLOYS

Ying Yang, Tianyi Chen, Lizhen Tan

Date Published: June 30, 2016

Prepared by
OAK RIDGE NATIONAL LABORATORY
Oak Ridge, TN 37831-6283
managed by
UT-BATTELLE, LLC
for the
US DEPARTMENT OF ENERGY
under contract DE-AC05-00OR22725

CONTENTS

Page

LIST OF FIGURES v
LIST OF TABLES vii
ACKNOWLEDGMENTS ix
EXECUTIVE SUMMARY xi
1. INTRODUCTION 1
2. COMPUTATIONAL THERMODYNAMICS AIDED ALLOY DESIGN 2
3. EXPERIMENTAL METHODS 4
4. RESULTS AND DISCUSSION 5
4.1 SEM characterizations 5
4.2 XRD characterizations 10
4.3 TEM characterizations 12
5. CONCLUSIONS AND FUTURE WORK 13
6. REFERENCES 14

LIST OF FIGURES

Figure 1. Calculated liquidus surface of (a)Fe-Cr-Zr and (b)Fe-Ni-Zr system 2
Figure 2. Isopleth section in the Fe-Cr-Ni-Zr system (a) fixed Cr at 13 at% and Zr at 33.3 at%, (b) fixed Cr at 13 at% and Ni at 5 at%. 3
Figure 3. Fe-Cr-Ni-Zr isothermal section at 1000 °C (black line) and 700 °C (red line) with Cr concentration being fixed at 12 wt%. The symbel denotes the alloy composition for experimental study. 3
Figure 4. BSE images of the four samples, (a) Z3N3, (b)Z6N5, (c)Z3N7 and (d)Z6N9, annealed at 700 °C for 1275 hours. 5
Figure 5. BSE images of the four samples, (a) Z3N3, (b)Z6N5, (c)Z3N7 and (d)Z6N9, annealed at 1000 °C for 336 hours. 6
Figure 6. EDS mappings of Z3N3, annealed at 700 °C for 1275 hours. (a) BSE image of the mapped region. (b) Fe mapping using Fe K-edge. (c) Cr mapping using Cr K-edge. (d) Ni mapping using Ni K-edge. (e) Zr mapping using Zr L-edge. 7
Figure 7. EDS mappings of Z3N7, annealed at 700 °C for 1275 hours. (a) BSE image of the mapped region. (b) Fe mapping using Fe K-edge. (c) Cr mapping using Cr K-edge. (d) Ni mapping using Ni K-edge. (e) Zr mapping using Zr L-edge. 7
Figure 8. EDS mappings of Z6N5, annealed at 700 °C for 1275 hours. (a) BSE image of the mapped region. (b) Fe mapping using Fe K-edge. (c) Cr mapping using Cr K-edge. (d) Ni mapping using Ni K-edge. (e) Zr mapping using Zr L-edge. 8
Figure 9. EDS mappings of Z6N9, annealed at 700 °C for 1275 hours. (a) BSE image of the mapped region. (b) Fe mapping using Fe K-edge. (c) Cr mapping using Cr K-edge. (d) Ni mapping using Ni K-edge. (e) Zr mapping using Zr L-edge. 8
Figure 10. (a) BSE image from Z6N9 sample annealed at 700 °C for 1275 hours. (b-d), EDS spectrums collected from the sites labeled as B, C and D in (a), respectively. The atomic percentages determined from Fe K-edge, Cr K-edge, Ni K-edge and Zr L-edge were printed on each spectrum. 9
Figure 11. XRD patterns of the samples annealed at 700 °C for 1275 hours. 11
Figure 12. XRD patterns of the samples annealed at 1000 °C for 336 hours. 11
Figure 13. (a) A TEM bright-field image of the Z3N7 sample annealed at 700 °C for 1275 hours. (b-e) SAD patterns of the grains labeled as B-E in (a), respectively. 12

LIST OF TABLES

Table 1. Nominal Compositions of the materials in this study (atomic %). 4
Table 2. Chemical compositions of each sample annealed at 700 °C for 1275 hours surveyed by EDS with SEM (atomic %). 10
Table 3. Chemical compositions of different phases in the Z3N7 sample annealed at 700 °C for 1275 hours. 13

ACKNOWLEDGMENTS

This research was sponsored by the U.S. Department of Energy (DOE), Office of Nuclear Energy (NE), the Nuclear Energy Enabling Technologies (NEET) program Reactor Materials FY 2015 Award. We gratefully acknowledge the support provided by Sue Lesica of DOE-NE and Stuart Maloy of Los Alamos National Laboratory.

The authors are grateful to David Harper and Tom Geer of Oak Ridge National Laboratory (ORNL) for alloy and sample preparation. Philip Maziasz of ORNL is appreciated for technical review of this report.

EXECUTIVE SUMMARY

Advanced nuclear reactors as well as the life extension of light water reactors require advanced alloys capable of satisfactory operation up to neutron damage levels approaching 200 displacements per atom (dpa). Extensive studies, including fundamental theories, have demonstrated the superior resistance to radiation-induced swelling in ferritic steels, primarily inherited from their body-centered cubic (bcc) structure. This study aims at developing nanoprecipitates strengthened advanced ferritic alloys for advanced nuclear reactor applications. To be more specific, this study aims at enhancing the ability for amorphization of Fe_2Zr-based nanoprecipitates in the Fe-Cr-Zr alloys through smart alloying strategy, and thereby promote the crystalline→amorphous transformation of these precipitates under irradiation.

With the aid of computational thermodynamics, Ni was identified to suppress the liquidus temperature of Fe_2Zr and four Fe-Cr-Ni-Zr alloys were designed to study the Ni effect on the phase stability of Fe_2Zr laves_phase. These alloys were fabricated through traditional arc-metling, followed by annealing at 1000 °C for 336 hours and 700 °C for 1275 hours. The microstructure were examined and characterized by SEM BSE image, EDS compositional mapping and point scan, XRD and TEM analysis. The major results were summarized below:

1) For investigated alloys with 12wt% Cr, 3~6wt% Zr and 3~9 wt%Ni, the phases in equilibrium with the BCC phase are C15_Laves phase, $Fe_{23}Zr_6$ phase. The volume fraction of intermetallic phases increases with Ni and Zr contents.
2) Instead of $(Fe,Cr)_2Zr$ C14_Laves phase, Ni stabilizes the C15_Laves structure in Fe-Cr-Ni-Zr alloys by substituting Fe and Cr atoms with Ni atoms in the first sublattice.
3) $Fe_{23}Zr_6$, that is metastable in the Fe-Cr-Zr ternary, is also stabilized by Ni addition.
4) Ni_7Zr_2 phase was observed in samples with high Ni/Zr ratio. Extensive solubility of Fe was identified in the phase.

The microstructural and composition results obtained from this study will be incorportated into the the Fe-Cr-Ni-Zr database. The current samples will be subjected to ion irradiaition to be compared with those results for Fe-Cr-Zr alloys. Additional alloys will be designed to form $(Fe,Cr,Ni)_2Zr$ nanoprecipitates for further studies.

1. INTRODUCTION

Advanced nuclear reactors as well as the life extension of light water reactors require advanced alloys capable of satisfactory operation up to neutron damage levels approaching 200 displacements per atom (dpa)[1]. Extensive studies, including fundamental theories, have demonstrated the superior resistance to radiation-induced swelling in ferritic steels, primarily inherited from their body-centered cubic (bcc) structure [2]. In our previous work [3], novel Fe-Cr-Zr ferritic alloys strengthened by Fe_2Zr_based Laves_phase precipitates show superior strength, ductility and creep resistance at high temperature, however, a consistent improvement on their irradiation resistance data have yet to be achieved. Amorphization of Fe_2Zr Laves phase has been frequently attained through mechanical alloying [4], sputtering deposition [5], and ion irradiation [6]. In a recent *in situ* ion irradiation study of a binary bcc(Fe)/Fe_2Zr nanocomposite, irradiation-induced amorphization of Fe_2Zr has been directly observed [7] under TEM. It was found that the density and size of the irradiation-induced defects such as dislocation loops is drastically low in the adjacent bcc matrix phase. In situ TEM revealed that the dislocation loops in Bcc(Fe) were confined by the crystal/amorphous interfaces and kept migrating to annihilate other defects. The amorphous Fe_2Zr nanolayer was also suggested as potential traps of the radiation-induced defects due to its excess free volume [7]. This study lends us new insights on the design of irradiation resistant Fe-Cr-Zr ferritic alloys.

Unlike the Fe_2Zr nanolayer in the Fe-Zr binary in literature [7], the Fe_2Zr nanoprecpitates formed in our Fe-Cr-Zr-based alloys still remain crystalline feature after irradiation. Preliminary TEM results clearly show the diffraction spots from crystalline Laves phase [8]. The lack of complete amorphization in our work can be attributed to several factors such as appreciable solubility of Cr in the Fe_2Zr phase, nonuniform sizes of Fe_2Zr particles, and unfavorable irradiation conditions. This incomplete amorphization can have a role in explaining the large scattering of the hardening data in the irradiated Fe-Cr-Zr-based (Z-) alloys [8]. While we could manipulate the irradiation conditions for complete amorphization, **we propose to enhance the ability for amorphization of Fe_2Zr-based nanoprecipitates in the Fe-Cr-Zr alloys through smart alloying strategy, and thereby promote the crystalline→amorphous transformation of these precipitates under irradiation.** With the enhanced ability for amorphization, the precipitates can better tolerate different irradiation conditions and size difference, and reach a complete crystalline→amorphous transformation.

The challenge is to identify smart alloying strategy that can promote the amorphous-forming ability of the $(Fe,Cr)_2Zr$ Laves precipitates. The concept of the amorphous-forming ability is borrowed from the glass-forming ability (GFA) of a melt [9]. While it is often evaluated by the critical cooling rate required to bypass the formation of crystals, it is primarily determined by the alloy composition. The GFA of an alloy composition has been gauged using the criterion of $T_x/(T_g+T_l)$, where T_x, T_l and T_g are the onset crystallization (solidus), liquidus and glass transition temperature, respectively. The larger the value of $T_x/(T_g+T_l)$, the higher the GFA. For a particular alloy system, the T_g does not differ very much from one composition to the other. In contrast, the T_x and T_l can change significantly with composition as suggested by solidus and liquidus of a phase diagram. Clearly, by reducing T_l, i.e., suppressing the liquidus temperature, the GFA can be improved. Extensive studies have suggested that the high GFA is closely related to large atomic size mismatch, large negative enthalpy of formation and complex crystal structure [10]. These conditions are often manifested in systems with low lying liquid surface, such as eutectic reaction [11-13].

2. COMPUTATIONAL THERMODYNAMICS AIDED ALLOY DESIGN

The selection of alloying elements and the design of experimental alloy compositions were aided by computational thermodynamics. The essence of computational thermodynamics, i.e., the CALPHAD (CALculation of PHAse Diagram) approach [14], was to construct phase diagrams of multicomponent systems based on well assessed thermodynamic functions of Gibbs energy of phases. In the prior NEET project, a thermodynamic database containing major elements of Fe, Cr, Zr and minor elements of Mo, W, Si, Nb, C has been developed and validated by experimental data [8]. Ni were also included in this database but need to be further validated by experimental data. This database is used as a starting point for alloy design. The experimental data generated from these alloys will be used to validate the calculated results.

Computation screening on isopleth of Fe_2Zr –Fe_2X (X=Mo, W, and Nb) found all these alloying elements increase the liquidus temperature of Fe_2Zr. In contrast, Ni addition into the Fe-Cr system decreases the liquidus temperature of Fe_2Zr. The major difference between Ni and other alloying elements such as Mo, Nb and W is that the former mainly substitutes the Fe in the first sublattice while the others substitute the Zr in the second sublattice. Therefore, Ni is selected as an element that has potential to promote the amorphous forming ability of Fe_2Zr. Based on the preliminary Fe-Cr-Zr-Ni database, we calculated the liquidus surface of the Fe-Cr-Zr and Fe-Ni-Zr and compared them side by side in Figure 1 (a) and (b). The results suggest the Fe-Ni-Zr liquidus surface is more suppressed than that of Fe-Cr-Zr.

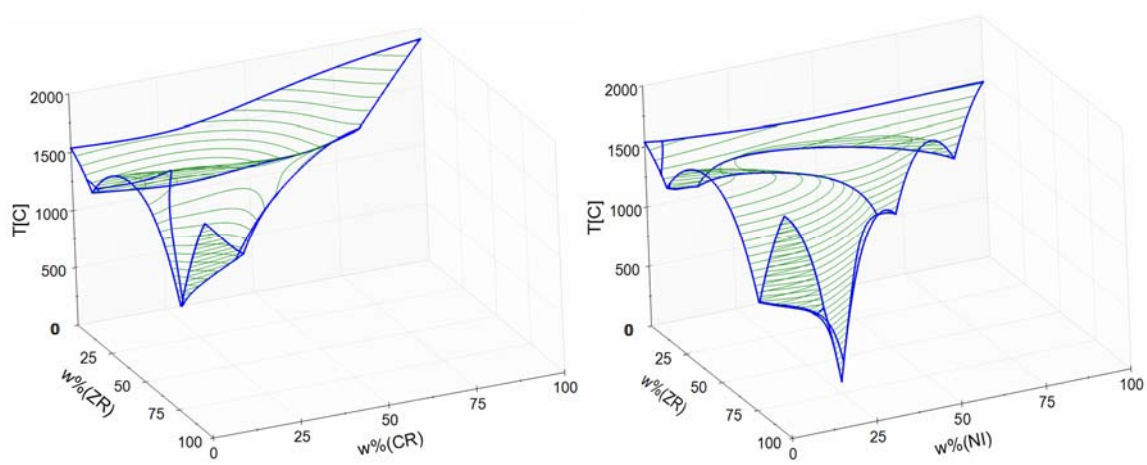

Figure 1. Calculated liquidus surface of (a)Fe-Cr-Zr and (b)Fe-Ni-Zr system

While it is difficult to visualize the liquidus surface in a quarternary system, we can plot different isopleth sections to see how Ni affects liquidus surface. Two isopleth section in the Fe-rich region were calculated and plotted in Figure 2 (a) and (b). One is the isopleth section with fixed Zr concentration at 33.3 at%. This isopleth essentially plots the phase diagram along M_2Zr (M=Fe,Cr, Ni) direction. We also need to fix another variable to obtain the 2D diagram. The Cr concentration is fixed at 12 wt%, as this amount of Cr is desired to reach desirable corrosion resistance. The results shows when increasing Ni concentration, the temperature of liquidus surface is decreasing. The second isopleth plots the phase diagram with fixed Cr and Ni concentration, in which a deep eutectic between Bcc(Fe) and Laves_C15 presents. Thermodynamic calculation suggests that adding Ni to the Fe-Cr-Zr alloy suppresses the liquidus surface in Fe-rich region, thus fufill our design goal. However, these results are exclusively from calculation. We

need to validate the calculation results from experiments. Isothermal sections of Fe-Cr-Ni-Zr at 1000 and 700°C were calculated with fixed Cr concention at 12 wt%. The calculated results are shown in Figure 3 with the red line denoting phase boundaries at 700°C, and the black line for 1000 °C.

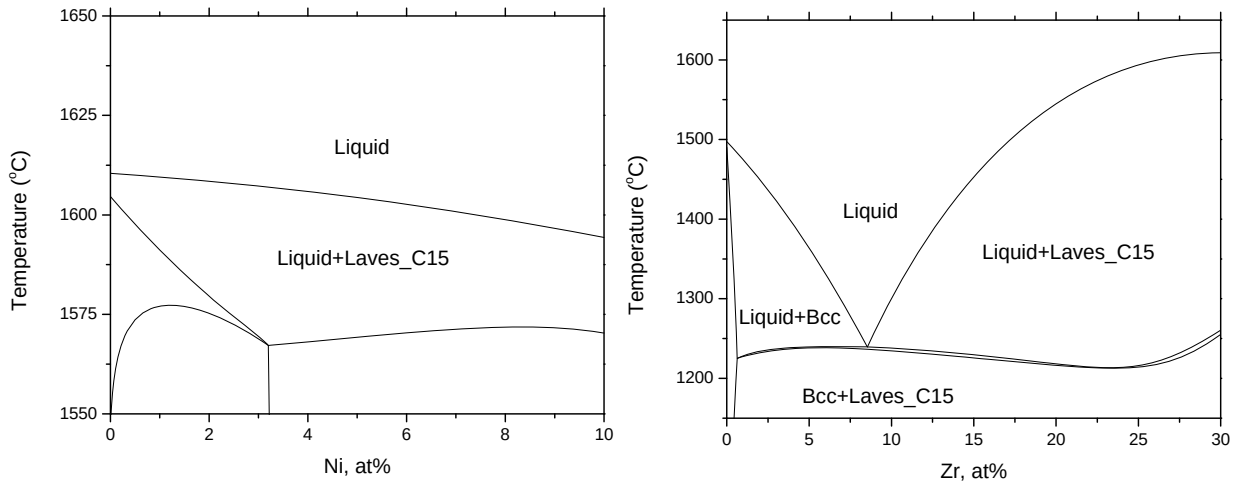

Figure 2. Isopleth section in the Fe-Cr-Ni-Zr system (a) fixed Cr at 13 at% and Zr at 33.3 at%, (b) fixed Cr at 13 at% and Ni at 5 at%.

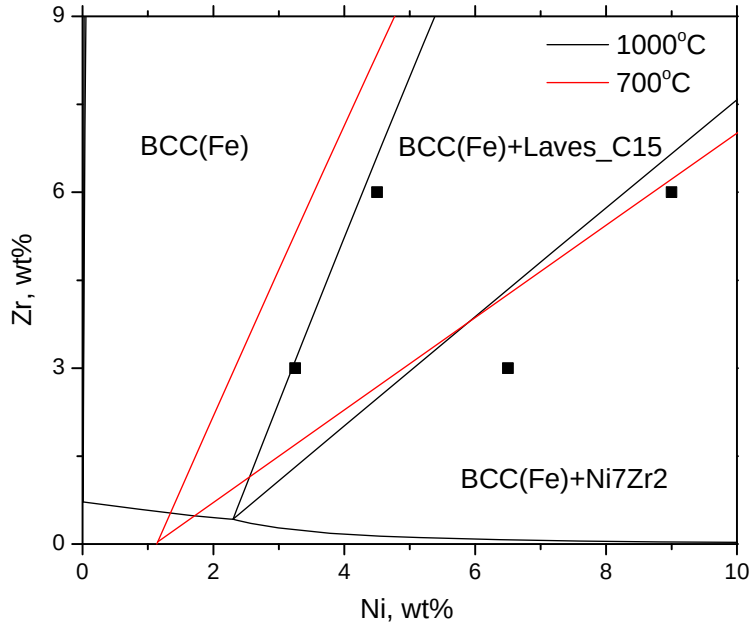

Figure 3. Fe-Cr-Ni-Zr isothermal section at 1000 °C (black line) and 700 °C (red line) with Cr concentration being fixed at 12 wt%. The symbel denotes the alloy composition for experimental study.

Four alloy compositions close to the phase boundary were selected for experimental study including

isothermal annealing at 1000 and 700 °C. Annealing at two temperatures can help us to get an idea how stable the phase boundary vs temperature and whether to introduce an entropy term when modeling the Gibbs energy function. The nominal alloy composition in wt% and at% are listed in Table 1.

Table 1. Nominal Compositions of the materials in this study (atomic %).

	Fe		Cr		Ni		Zr	
	At%	Wt%	At%	Wt%	At%	Wt%	At%	Wt%
Z3N3	82.11	81.75	12.94	12	3.11	3.25	1.84	3
Z3N7	78.97	78.5	12.96	12	6.22	6.5	1.85	3
Z6N5	78.81	77.5	13.11	12	4.35	4.5	3.73	6
Z6N9	74.40	73	13.13	12	8.73	9	3.74	6

3. EXPERIMENTAL METHODS

The starting materials are elemental Fe, Cr, Zr and Ni with purity level as >99.904%, >99.978%, >99.2% and >99.15%, respectively. Small buttons of each alloy, with a target weight of 10 g, were produced by arc-melting in a pure Ar atmosphere. The total weight loss was less than 0.01%, therefore, the alloys were considered as having the nominal compositions.

Each button was cut into three pieces. One of them was used for as-cast microstructure analysis and the other two were capsuled in evacuated quartz tubes and annealed at 1000 °C for 336 hours and 700 °C for 1275 hours, respectively. After the heat treatment, the annealed samples were quenched to room temperature with water.

The samples were mechanically polished for scanning electron microscope (SEM) based characterizations. A JEOL 6500F and a Hitachi S4800 SEM were used for backscattering electron microscopy (BSE) and energy-dispersive X-ray spectroscopy (EDS). Both SEM have the field emission systems and the guns were operated at acceleration voltages of 20 kV. X-ray diffraction (XRD) analysis was also conducted on the annealed samples for phase identification. A Bruker D2 phaser with Cu Kα radiation (λ=1.54056 Å) was used to carry out the scanning over a range of 30 °-60 ° in 2θ. The step size was set to be 0.02 °. At each step, the diffracted X-ray was collected for 40 seconds. Transmission electron microscopy (TEM) was used to characterize one of the four samples. Selected area electron diffraction (SAD) patterns were used to furtherly confirm the phase identifications. More accurate chemical compositions of each phase were obtained using EDS. The TEM used in this study is a JEOL 2100F operated at 200 kV. TEM samples were prepared using focused-ion-beam (FIB) technique with a FEI versa 3D SEM/FIB dual beam system.

4. RESULTS AND DISCUSSION

4.1 SEM characterizations

The SEM BSE image and EDS were used to analyze the morphology and composition of phases in the invesitigated alloys. Figures 4 and 5 show the BSE images of the four samples annealed at 700 °C and 1000 °C for 1275 hours, respectively. The Fe-based matrix has a darker contrast while the intermetallic phases, containing higher level of Zr, are brighter in the BSE images. In Figure 4, eutectic microstructures with fine features of ~0.5 µm (for instance the inset of Figure 4c) were observed in the samples annealed at 700 °C. Based on the BSE image analysis results, the fractions of the intermetallic phases in all the four samples are estimated to be 10%, 13%, 20% and 20% for Z3N3, Z3N7, Z6N5 and Z6N9 samples, respectively. Higher Zr content leads to higher fraction of intermetallic phases. EDS results show that the compositions of three intermetallic phases, namely Fe_2Zr, $Fe_{23}Zr_6$ and Ni_7Zr_2, observed in the set of Fe-Cr-Zr-Ni samples.

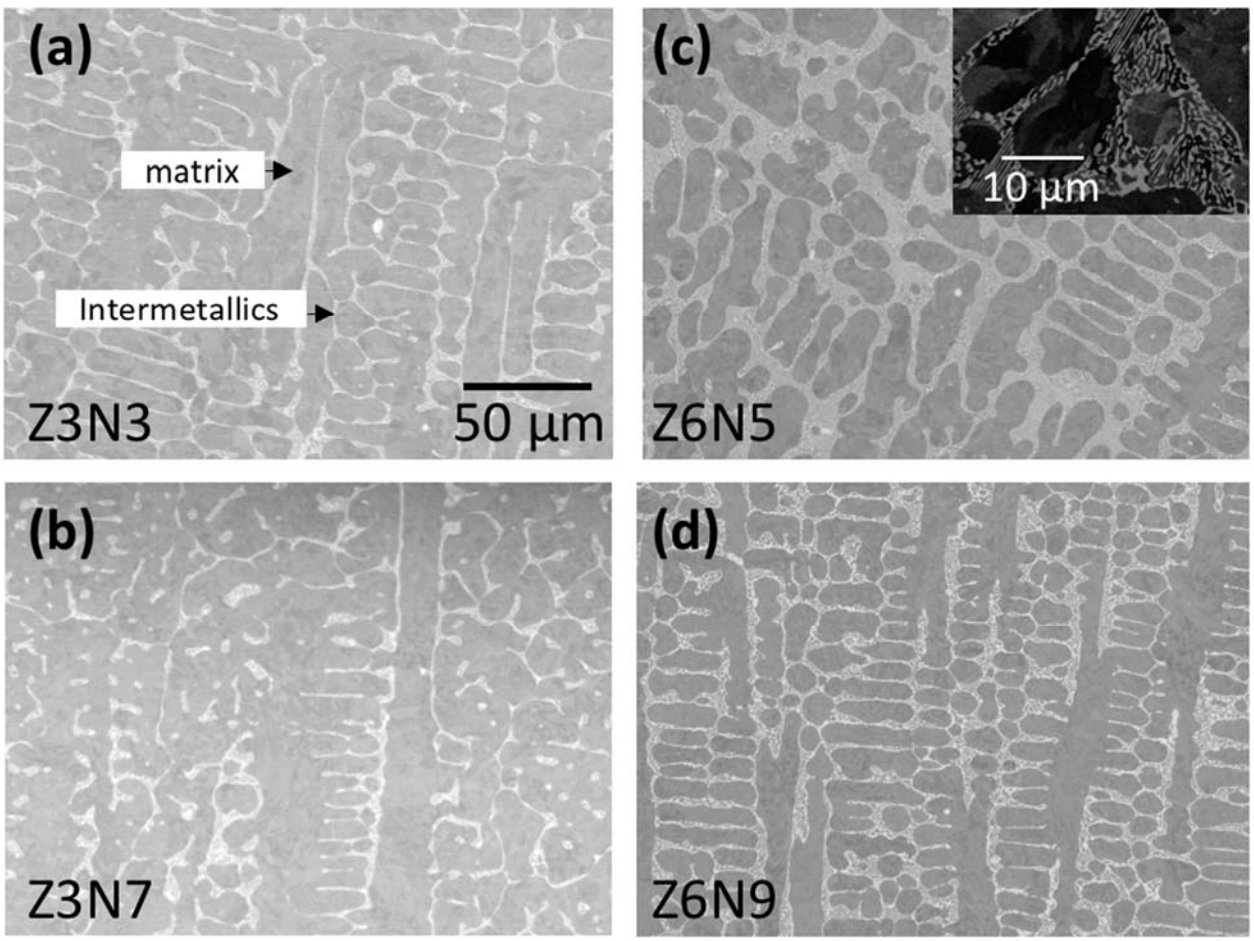

Figure 4. BSE images of the four samples, (a) Z3N3, (b)Z6N5, (c)Z3N7 and (d)Z6N9, annealed at 700 °C for 1275 hours.

The microstructure of the samples after annealing at 1000 °C for 336 hours are shown in Figure 5. In comparison with the micrographs in Figure 4, no significant change of the overall fraction of the intermetallic phases were found from the estimations on the samples annealed at 700 °C. This suggests that the phase boundaries do not significantly change over the range of temperatures. However, eutectic

microstructures after annealed at 1000 °C show coarser features than those at 700°C. This difference is demonstrated by the comparison between the inserted figures in Figure 4c and Figure 5d. This result suggests that the kinetics of the alloys at 700°C is not fast enough and the fine eutectic in the as-cast microstructure still remains after 1275-hour annealing. In contrast, coarsening due to the fact kinetics at 1000°C leads to the microsturuture more towards the equilibrium state. However, even for the samples annealed at 1000 °C, fine features were still visible in Figure 5b and 5d, suggesting that equilibrium was not fully reached even after thermal annealing at 1000 °C for 336 hours.

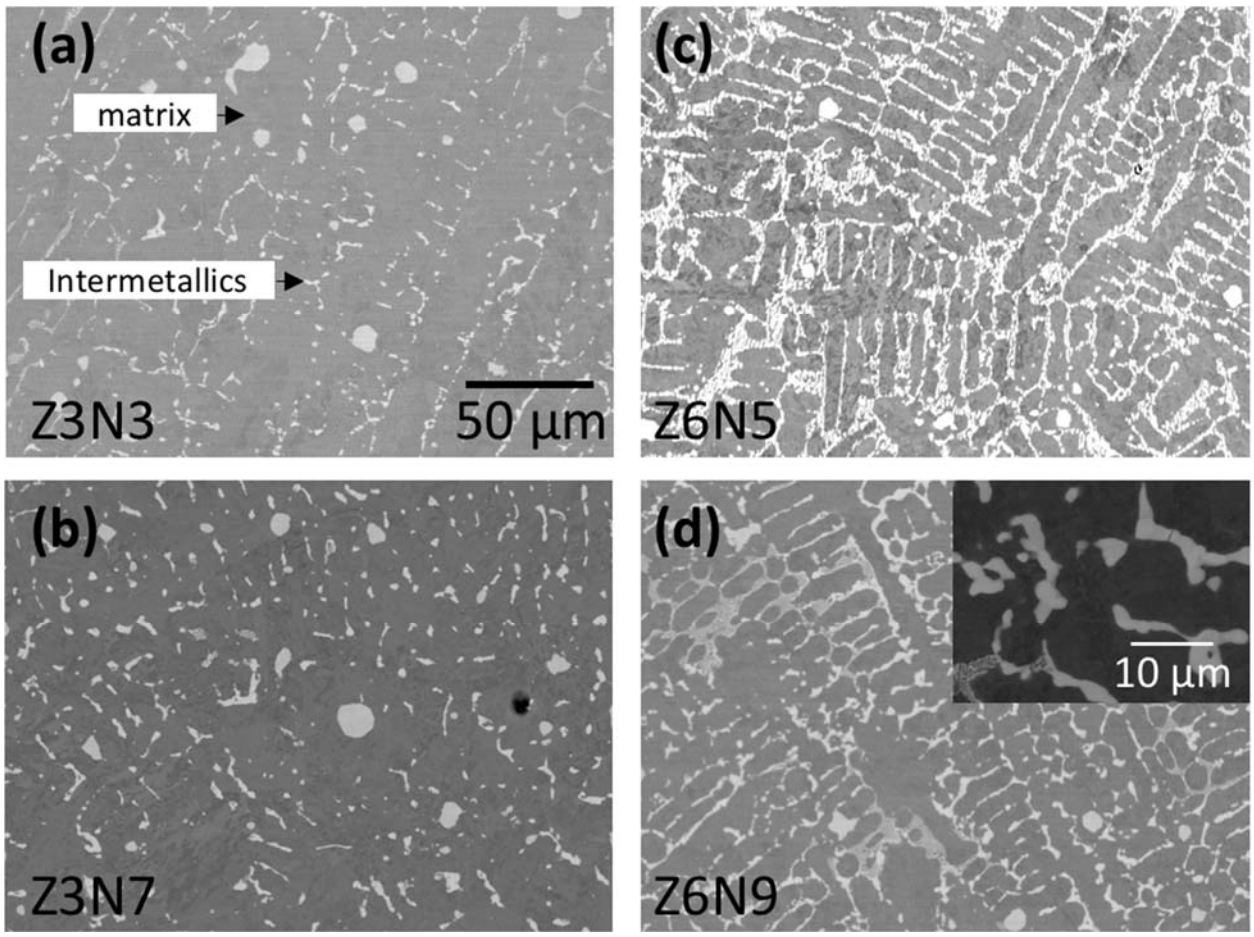

Figure 5. BSE images of the four samples, (a) Z3N3, (b)Z6N5, (c)Z3N7 and (d)Z6N9, annealed at 1000 °C for 336 hours.

The chemical compositions of the samples were studied using SEM EDS techniques. Figure 6–9 show EDS mapping results of the samples of Z3N3, Z3N7, Z6N5 and Z6N9, respectively, which were annealed at 700 °C. The elemental distributions of Fe, Cr, Zr and Ni were obtained using FeK, CrK, ZrL and NiK signals, respectively. Overall, the intermetallic phases formed in the set of quaternary alloys are rich in Zr and Ni, while the matrix phase is rich in Fe and Cr and lean in Zr and Ni. Among the intermetallic phases, Ni and Zr are not uniformly distributed, as seen from Figure 6–9 in (d) and (e). Particularly, the Ni concentrated phases are very obvious, suggesting the presence of a Ni-dominant phase. Qualitatively, the fraction of the Ni-dominant phase is correlated to the ratio of the compositions of Ni and Zr rather than the absolute compositions of Zr. None of the Ni-dominant phase was observed in the sample of Z6N5, with the

lowest ratio of Ni to Zr. On the other hand, the Ni-dominant phase was more frequently observed in the samples of Z6N9 and Z3N7, where the Ni-Zr ratios are higher.

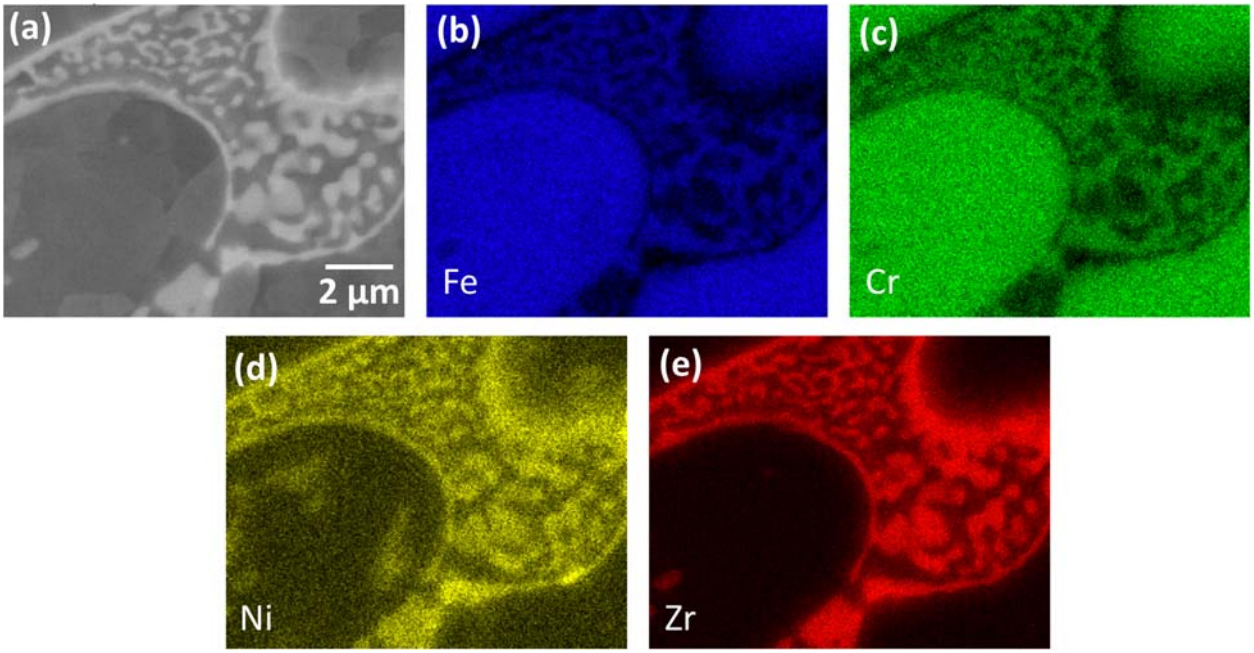

Figure 6. EDS mappings of Z3N3, annealed at 700 °C for 1275 hours. (a) BSE image of the mapped region. (b) Fe mapping using Fe K-edge. (c) Cr mapping using Cr K-edge. (d) Ni mapping using Ni K-edge. (e) Zr mapping using Zr L-edge.

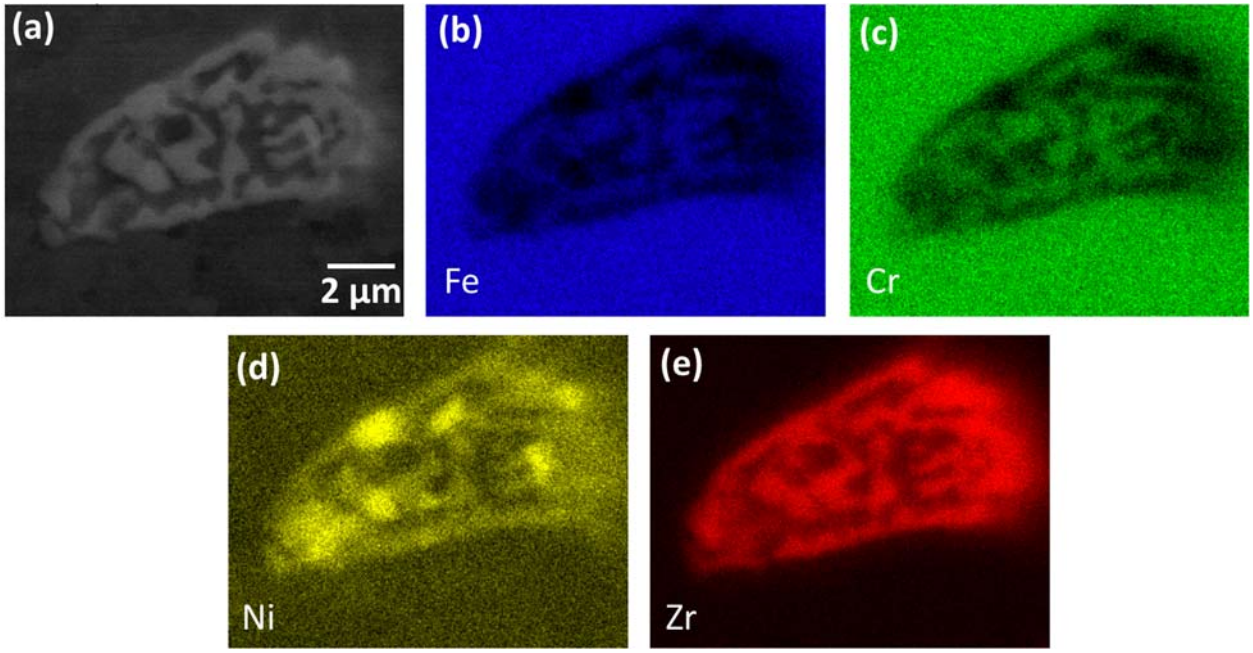

Figure 7. EDS mappings of Z3N7, annealed at 700 °C for 1275 hours. (a) BSE image of the mapped region. (b) Fe mapping using Fe K-edge. (c) Cr mapping using Cr K-edge. (d) Ni mapping using Ni K-edge. (e) Zr mapping using Zr L-edge.

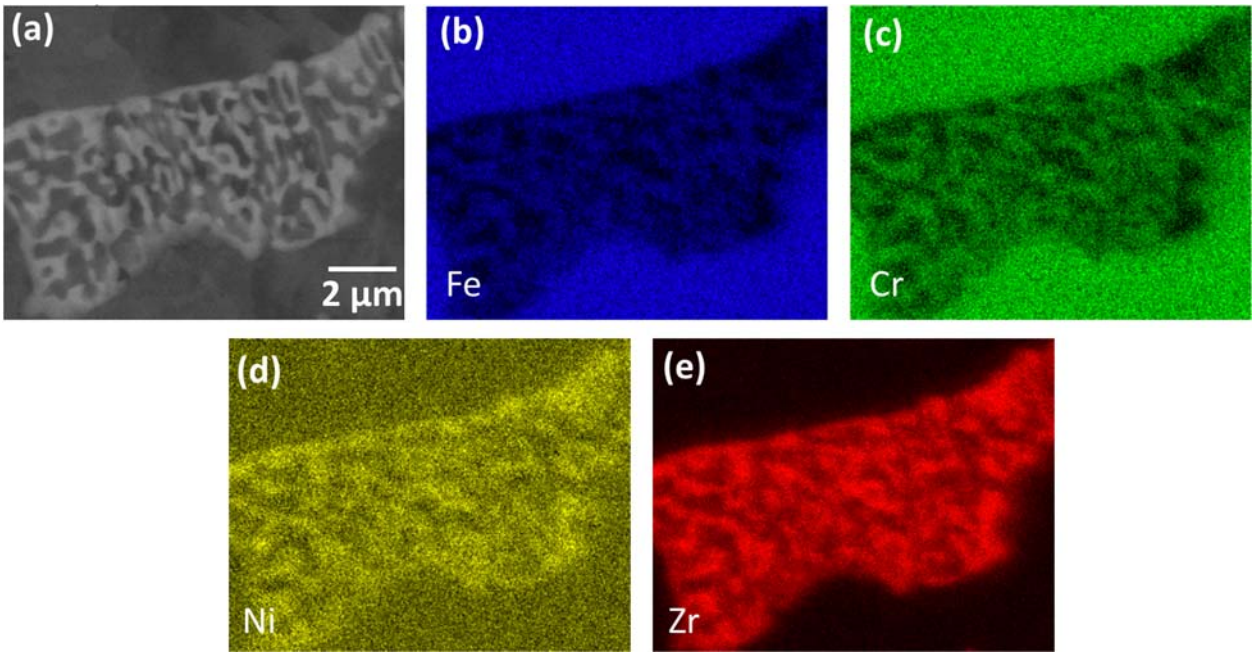

Figure 8. EDS mappings of Z6N5, annealed at 700 °C for 1275 hours. (a) BSE image of the mapped region. (b) Fe mapping using Fe K-edge. (c) Cr mapping using Cr K-edge. (d) Ni mapping using Ni K-edge. (e) Zr mapping using Zr L-edge.

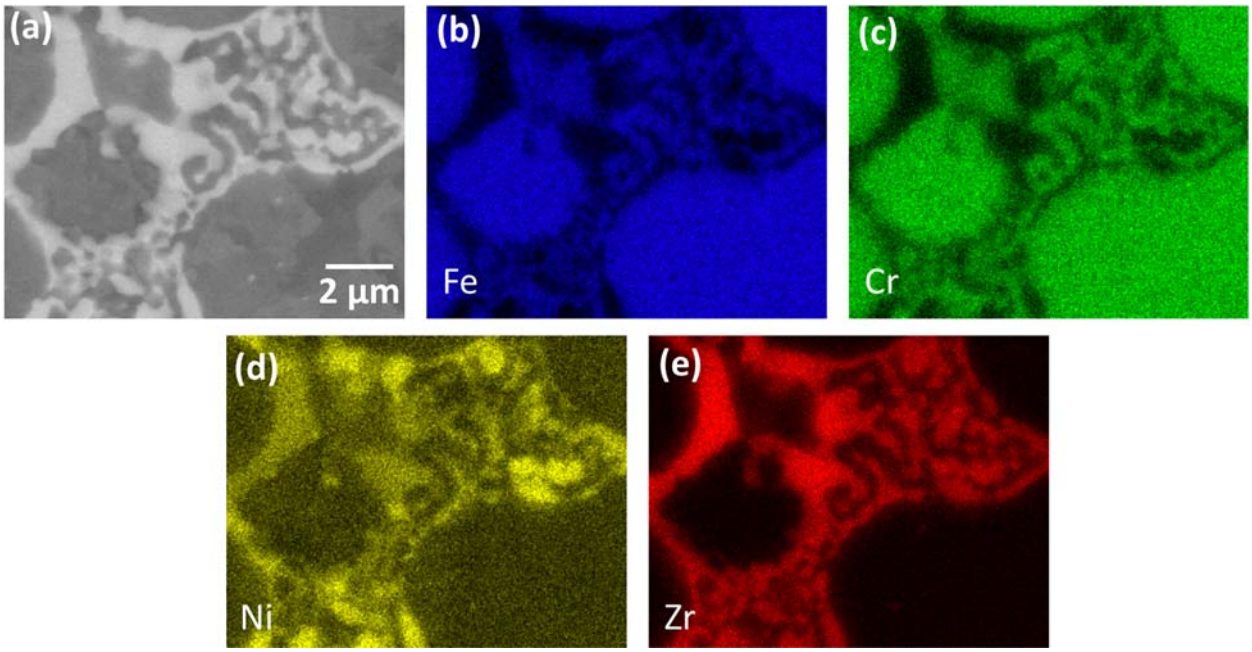

Figure 9. EDS mappings of Z6N9, annealed at 700 °C for 1275 hours. (a) BSE image of the mapped region. (b) Fe mapping using Fe K-edge. (c) Cr mapping using Cr K-edge. (d) Ni mapping using Ni K-edge. (e) Zr mapping using Zr L-edge.

The results of EDS point surveys from the sample Z6N9 annealed at 700°C are shown in Figure 10. The EDS spectrums obtained from the sites of B, C and D are shown in Figure 10 (b), (c), and (d), respectively. Site B is in the matrix phase, which is a Fe-Cr compound with small amount of Ni and Zr solutes, as suggested by the EDS analysis. Spectrums in Figure 10 (c) and (d) were obtained from the intermetallic phases, with the characteristic high fractions of Zr and Ni. Given that the feature sizes of the intermetallic phases are smaller than the interaction volume of 20 keV electron (with the latter having a typical dimension of ~5 µm), the composition estimated from sites C and D were inevitably influenced by their surroundings. Still, qualitatively, the intermetallic phase at D has a higher Ni-Zr ratio than the intermetallic phase at C. As will be shown later, the low Ni phase corresponds to either $(Fe,Ni)_2Zr$ or $(Fe,Ni)_{23}Zr_6$, and the high Ni phase corresponds to $(Ni,Fe)_7Zr_2$. The results of EDS point surveys done with SEM on the samples annealed at 700 °C are compelled in Table 2. As will be discussed later, the EDS analysis done with SEM is not accurate due to the relatively large beam size compared with the sizes of the features of intersts. Yet, the differences in composition among the matrix and intermetallic phases are obvious.

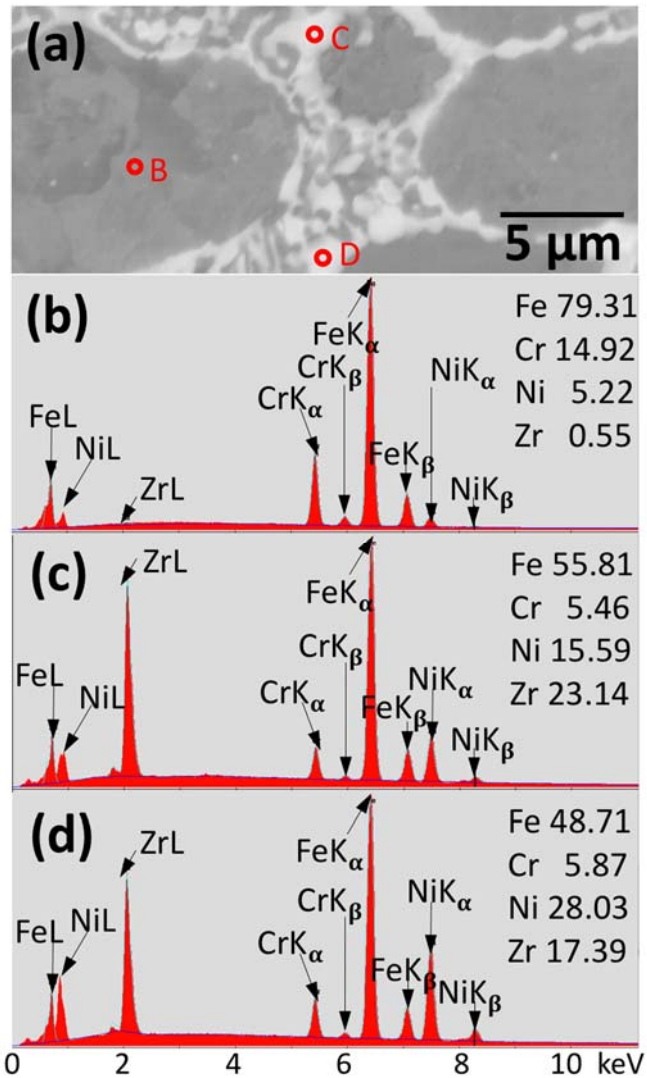

Figure 10. (a) BSE image from Z6N9 sample annealed at 700 °C for 1275 hours. (b-d), EDS spectrums collected from the sites labeled as B, C and D in (a), respectively. The atomic percentages determined from Fe K-edge, Cr K-edge, Ni K-edge and Zr L-edge were printed on each spectrum.

Table 2. Chemical compositions of each sample annealed at 700 °C for 1275 hours surveyed by EDS with SEM (atomic %).

	Matrix	$(Fe,Ni)_2Zr$ or $(Fe,Ni)_{23}Zr_6$	$(Ni,Fe)_7Zr_2$
Z3N3	Fe: 84.59 ± 0.17 Cr: 13.58 ± 0.07 Ni: 1.41 ± 0.14 Zr: 0.42 ± 0.05	Fe: 69.92 ± 0.52 Cr: 8.84 ± 0.42 Ni: 7.49 ± 0.34 Zr: 13.75 ± 0.43	Fe: 63.40 ± 0.13 Cr: 7.85 ± 0.86 Ni: 13.53 ± 1.64 Zr: 15.24 ± 2.63
Z3N7	Fe: 80.36 ± 0.26 Cr: 13.99 ± 0.11 Ni: 5.08 ± 0.19 Zr: 0.56 ± 0.19	Fe: 58.30 ± 1.16 Cr: 5.86 ± 1.07 Ni: 13.65 ± 0.85 Zr: 21.74 ± 1.52	Fe: 51.26 ± 0.62 Cr: 6.35 ± 0.55 Ni: 25.04 ± 1.68 Zr: 17.36 ± 2.85
Z6N5	Fe: 81.78 ± 0.18 Cr: 14.26 ± 0.20 Ni: 3.55 ± 0.47 Zr: 0.41 ± 0.16	Fe: 67.61 ± 1.31 Cr: 9.21 ± 0.48 Ni: 7.33 ± 0.84 Zr: 15.85 ± 1.12	-
Z6N9	Fe: 78.37 ± 0.79 Cr: 14.81 ± 0.06 Ni: 6.06 ± 0.55 Zr: 0.58 ± 0.04	Fe: 55.16 ± 1.20 Cr: 5.09 ± 0.76 Ni: 16.4 ± 0.60 Zr: 23.25 ± 1.75	Fe: 49.35 ± 2.39 Cr: 6.01 ± 1.30 Ni: 27.14 ± 1.51 Zr: 17.44 ± 2.25

4.2 XRD characterizations

The XRD patterns of the samples annealed at 700 °C and 1000 °C are shown in Figure 11 and 12, respectively. The strongest peaks near 2θ=44.56 ° corresponds to the (110) of body-centered-cubic (BCC) Fe-Cr, the matrix phase. The other peaks, labeled as C15 and $Fe_{23}Zr_6$, corresponds to the Fe_2Zr Laves phase with cubic C15 structure and the $Fe_{23}Zr_6$ phase. The peaks corresponding to the C15 and $Fe_{23}Zr_6$ phases were observed in all samples subjected to both annealing conditions, suggesting that they are both stable at the temperatures of 700°C and 1000 °C. Considering their relative peak intensity changes in different samples with variant compositions, it seems that $Fe_{23}Zr_6$ is at a higher fraction of the intermetallic phases when the material contains a smaller amount Zr. No peaks of the C14 or C36 of the Laves phase was observed under the experiment conditions of this study. A standard XRD pattern of LaB_6, which was shown associated with the Z6N9 pattern in Figure 12, was used to calibrate the 2θ measurements. Using the Bragg's formula, the lattice parameters of the C15 Laves phase and the $Fe_{23}Zr_6$ phase were estimated to be 6.98 Å and 11.69 Å, respectively.

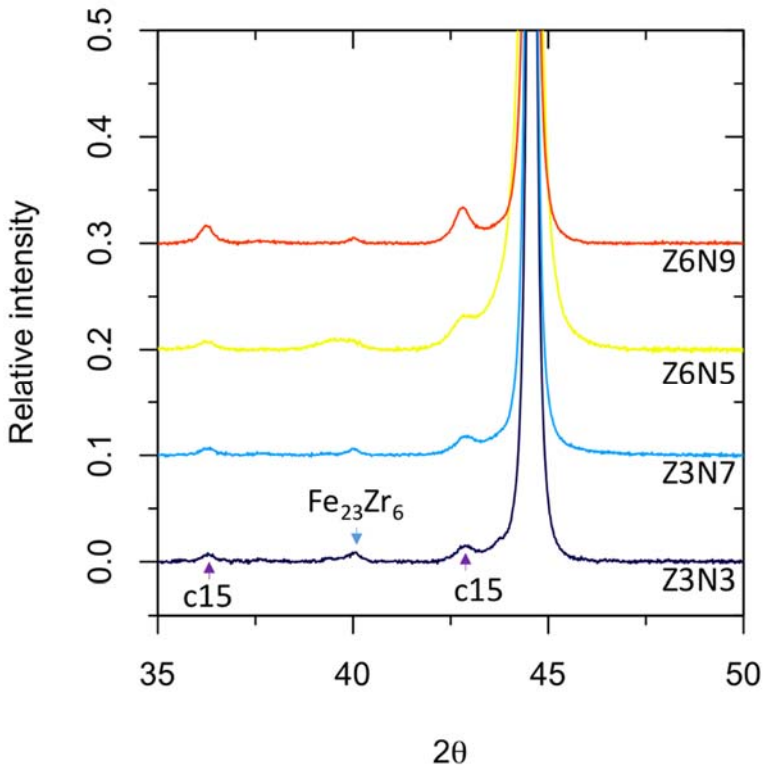

Figure 11. XRD patterns of the samples annealed at 700 °C for 1275 hours.

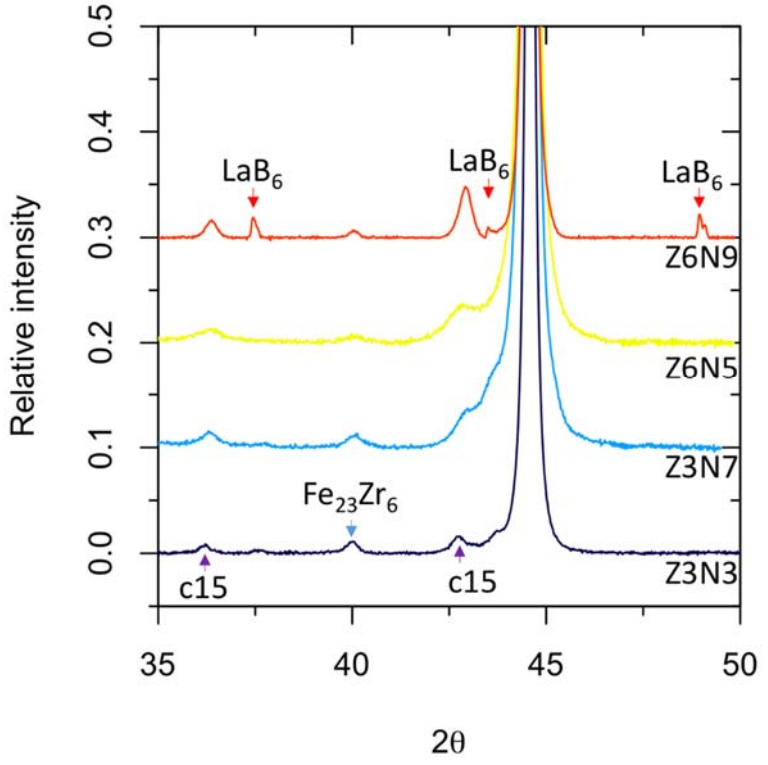

Figure 12. XRD patterns of the samples annealed at 1000 °C for 336 hours.

In the earlier study of Fe-Cr-Zr ternary systems, Cr was found to enhance the formation of hexagonal Laves phase (C14 or C36) against the cubic Laves phase (C15) [15]. As a result, in a Fe-12.5Cr-10Zr system, peaks of C14/C36 were observed in XRD patterns instead of C15. However as shown in Figure 11 and 12 in this study, the Laves phase formed in the Fe-Cr-Zr-Ni systems favors C15 structure. In addition, based on the EDS analysis reported in Figure 6–9, there is considerable amount of Ni mixed in the C15 Laves phase. Given that Ni has smaller atomic radius than Fe does, the $(Fe,Ni)_2Zr$ C15 structure has lattice parameter smaller than that of the C15 Fe_2Zr Laves phase [16]. The mixture of Ni into the Laves phase is believed to stabilize the C15 structure over a temperature up to 1000 °C, as shown in the experimental results in this study.

Similar to the C15 Laves phase, $Fe_{23}Zr_6$ was observed in the temperature range of 700-1000 °C. Ni was also found to be the solute, forming $(Fe,Ni)_{23}Zr_6$. In Fe-Zr binary system, $Fe_{23}Zr_6$ has been found to contain up to 1 w.% O and thus considered as an oxygen-stabilized phase [17]. In Fe-Cr-Zr ternary system, the thermodynamic modeling showed that only a very small amount of energy (0.68 KJ/mole atoms) change is in need for $Fe_{23}Zr_6$ to become s stable phase [15]. In the Fe-Cr-Zr-Ni quaternary system, XRD investigations show considerable amount of $(Fe,Ni)_{23}Zr_6$ observed in all experimental conditions in this study. Given the observations in this study, as well as previous considerations in the binary and ternary systems, it is very possible that $(Fe,Ni)_{23}Zr_6$ is a stable phase in the Fe-Cr-Zr-Ni system. The addition of Ni to the $Fe_{23}Zr_6$ could stabilize it by providing multiple possible sites for the transition-metal elements with different atomic environments and associated volumes [18].

4.3 TEM characterizations

Figure 13 shows the results from TEM investigation of the Z3N7 sample after annealed at 700 °C for 1275 hours. As shown in Figure 13a, grains of 0.5 µm in size were observed in the eutectic microstructures. Analysis of SAD patterns revealed that these grains with similar sizes have different crystal structures. The domain C was found to be the matrix phase, having a BCC crystal structure. The crystal structures of domains B and E are the C15 Laves structure and the $Fe_{23}Zr_6$ structure, respectively. The observations of these two crystal structures show agreement to the XRD results. Domain D was found to have a Ni_7Zr_2 C12 structure, which was not marked in the XRD patterns in Figures 11–12 because of the overlapping of the strongest peak of the Ni_7Zr_2 with the (110) peak of BCC.

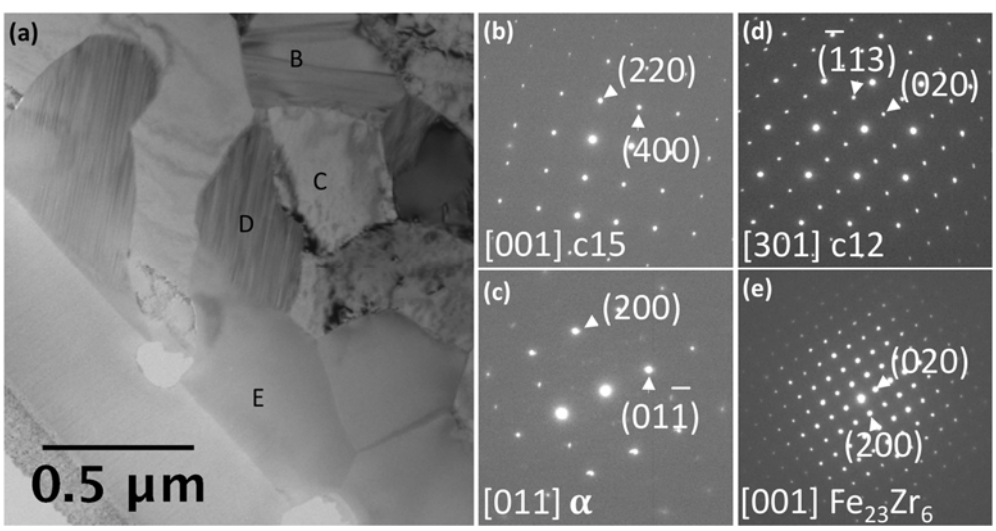

Figure 13. (a) A TEM bright-field image of the Z3N7 sample annealed at 700 °C for 1275 hours. (b-e) SAD patterns of the grains labeled as B-E in (a), respectively.

The chemical compositions of each labeled domains in Figure 13a were determined using EDS technique. The averaged atomic percentages of Fe, Cr, Ni and Zr for each domain were listed in Table 3. Qualitatively, the chemical composition determined using TEM is in agreement with the estimation using SEM, which is shown in Figure 11. Given that the beam spot is much smaller in TEM, the EDS analysis from TEM is considered to be more accurate. With this accuracy, the compositions of the all three intermetallic phases found in current study are distinctive. The solublity of each intermetallic phase can be estimated. The Ni_7Zr_2 phase was found to be the Ni-rich phase as shown in the EDS mappings in Figure 6–9. Based on the compositions shown in Table 3, the formula of this phase is $(Ni_{0.5}Fe_{0.5})_7Zr_2$. The formulas of the Fe_2Zr and $Fe_{23}Zr_6$ phases, as determined in the same manner, are $(Fe_{0.7}Ni_{0.3})_2Zr$ and $(Fe_{0.8}Ni_{0.2})_{23}Zr_6$, respectively.

Table 3. Chemical compositions of different phases in the Z3N7 sample annealed at 700 °C for 1275 hours.

	Fe (at.%)	Cr (at.%)	Ni (at.%)	Zr (at.%)
BCC phase	84.59 ± 0.16	13.79 ± 0.37	1.49 ± 0.09	0.12 ± 0.25
Fe_2Zr C15	49.82 ± 2.36	1.49 ± 0.18	17.49 ± 0.31	31.20 ± 2.84
$Fe_{23}Zr_6$	62.67 ± 0.33	4.01 ± 0.10	12.96 ± 0.55	20.37 ± 0.78
Ni_7Zr_2 C12	37.43 ± 2.00	0.91 ± 0.24	37.05 ± 0.35	24.63 ± 1.89

5. CONCLUSIONS AND FUTURE WORK

With the aid of computational thermodynamics, Ni was identified to suppress the liquidus temperature of Fe_2Zr and four Fe-Cr-Ni-Zr alloys were designed to study the Ni effect on the phase stability of Fe_2Zr laves_phase. These alloys were fabricated through traditional arc-metling, followed by annealing at 1000°C for 336 hours and 700°C for 1275 hours. The microstructure were examined and characterized by SEM BSE image, EDS compositional mapping and point scan, XRD and TEM analysis. The major results were summarized below:

5) For investigated alloys with 12wt% Cr, 3~6wt% Zr and 3~9 wt%Ni, the phases in equilibrium with the BCC phase are C15_Laves phase, $Fe_{23}Zr$ phase. The volume fraction of intermetallic phases increases with Ni and Zr contents.
6) Instead of $(Fe,Cr)_2Zr$ C14_Laves phase, Ni stabilizes the C15_Laves structure in Fe-Cr-Ni-Zr alloys by substituting Fe and Cr atoms with Ni atoms in the first sublattice.
7) $Fe_{23}Zr_6$, that is metastable in the Fe-Cr-Zr ternary, is also stabilized by Ni addition.
8) Ni_7Zr_2 phase was observed in samples with high Ni/Zr ratio.

The microstructural and composition results obtained from this study will be incorportated into the the Fe-Cr-Ni-Zr database. The current samples will be subjected to ion irradiaition to be compared with those results for Fe-Cr-Zr alloys. Additional alloys will be designed to form $(Fe,Cr,Ni)_2Zr$ nanoprecipitates for further studies.

6. REFERENCES

[1] Zinkle SJ, Snead LL. Annual Review of Materials Research 2014;44:241.

[2] Raj B, Vijayalakshmi M. RJM Konings, TR Allen, RE Stoller, S. Yamanaka, Comprehensive Nuclear Materials, Elsevier 2012.

[3] Tan L, Yang Y. Metallurgical and Materials Transactions A 2015;46:1188.

[4] Hellstern E, Schultz L. Materials Science and Engineering 1988;97:39.

[5] Castaño F, Stobiecki T, Gibbs M, Czapkiewicz M, Kopcewicz M, Gacem V, Speakman J, Cowlam N, Blythe H. Journal of Physics: Condensed Matter 1997;9:10603.

[6] Byeli A, Kukareko V, Kononov A, Bilenko E. Journal of Surface Investigation. X-ray, Synchrotron and Neutron Techniques 2008;2:340.

[7] Yu K, Fan Z, Chen Y, Song M, Liu Y, Wang H, Kirk M, Li M, Zhang X. Materials Research Letters 2015;3:35.

[8] Tan L. Development and Mechanical Results of Zr-Bearing Ferritic Steels. Oak Ridge National Laboratory (ORNL), 2015.

[9] Lu Z, Liu C. Acta materialia 2002;50:3501.

[10] Takeuchi A, Inoue A. Materials Transactions 2005;46:2817.

[11] Johnson WL. Fundamental aspects of bulk metallic glass formation in multicomponent alloys. Materials science forum, vol. 225: Trans Tech Publ, 1996. p.35.

[12] Ma D, Cao H, Ding L, Chang YA, Hsieh K, Pan Y. Applied Physics Letters 2005;87:171914.

[13] Yan X-Y, Chang Y, Yang Y, Xie F-Y, Chen S-L, Zhang F, Daniel S, He M-H. Intermetallics 2001;9:535.

[14] Kaufman L, Bernstein H. 1970.

[15] Yang Y, Tan L, Bei H, Busby JT. Journal of Nuclear Materials 2013;441:190.

[16] Muraoka Y, Shiga M, Nakamura Y. physica status solidi (a) 1977;42:369.

[17] Stein F, Sauthoff G, Palm M. Journal of Phase Equilibria 2002;23:480.

[18] Ohodnicki Jr P, Cates N, Laughlin D, McHenry M, Widom M. Physical Review B 2008;78:144414.